Mathematical model depicting the deposition kinetics process into rf-magnetron co-sputtering of strontium barium titanate thin films

J. Reséndiz-Muñoz [a], M. T. Zagaceta-Álvarez [b], J. L. Fernández-Muñoz [c*], M. A. Gruintal-Santos [d]

[a] *Q&P Consulting, Justo Sierra S/N, Col. Santa Bárbara, Azcapotzalco, Z.P. 02230, CDMX México.*

[b] *Higher School of Mechanical and Electrical Engineering (ESIME-IPN-AZ), Azcapotzalco Unit, National Polytechnic Institute, Av. Granjas, Mexico City, Z.P.02250, México.*

[c] *National Polytechnic Institute, CICATA-IPN Legaria Unit, Legaria 694 Avenue, Col. Irrigación, Miguel Hidalgo, Z.P. 11500 Mexico City, México.*

[d] *Autonomous University of Guerrero, Faculty of Agricultural and Environmental Sciences. Master in Agricultural Sciences and Local Management. Tuxpan Unit, km 2.5 Carretera Iguala-Tuxpan, Iguala de la Independencia, Guerrero, México. Z.P.40101.*

Thin films deposition kinetics of $Ba_XSr_{1-X}TiO_3$ (BST)/nichrome is modeled by the stoichiometric rate of a perovskite-type material such as ABO_3, where cations *A*, *B*, and the anion oxygen should ideally have a 1:1:3 rate, respectively. The experimental stoichiometry data measured by EDS on films of 240 nm, and the *Ba/Sr*, *(Ba+Sr)/Ti* rates considered in percentages starting from arithmetic and the sigmoidal relationship between *Ba* and *Sr*. They show relationships in sigmoidal, exponential, and parabolic mathematical functions that together describe the BST thin films deposition kinetics by means of RF-Magnetron Co-Sputtering (RFMCS). The proposed mathematical model is fundamental to optimize, explain and use the deposition process working conditions, such as the working pressure, the Ar/O_2 rate in percentage, and sccm. The controlled applied power on each $BaTiO_3$ (BTO) and $SrTiO_3$ (STO) targets achieve more accurate stoichiometry in thin films deposition for solid solutions on quaternary materials.

Keywords: Sputtering deposition, thin films, stoichiometric behavior, barium strontium titanate, deposition kinetics.

(Received April 14, 2021; Accepted January 6, 2022)

1. Introduction

Recent research has shown that in the BST thin films deposition process by means of RFMCS when complementary and simultaneous applied powers used in two magnetrons, *Ba* and *Sr* are depositions on the substrate following a mathematical sigmoidal form. That is, the concentration follows a sigmoidal S-profile equation as a function of the complementary applied power on non-stoichiometric targets of $BaTiO_3$ (BTO) and $SrTiO_3$ (STO) [1,2,3]. This sigmodal mathematical model and the fit with experimental data measured by EDS and XRD has been used to explain the chemical structure and some properties such as: the gap energy, the deposition rate, the crystal size, and the resistivity of the BST on quartz substrates for different temperatures. Also, the relationship with the amorphous or crystalline structure and with deposition areas rich in some of the cations of the BST solid solution (*Ba*-rich or *Sr*-rich) [1-7]. In other types of research, the *Ba/Sr*, *(Ba+Sr)/Ti*, *Ba/Ti*, *Sr/Ti* ratios have been scrupulously studied in relation to properties such as: electrical, dielectric, and optical. The way in which the change in the flow of gases (Ar/O_2, $O_2/(Ar+O_2)$, $(Ar+O_2)$ (and its relationship with the working pressure or total chamber gas pressure,

* Corresponding author: jlfernandez@ipn.mx
https://doi.org/10.15251/DJNB.2022.171.1

or the pressure partial oxygen) in the RFMCS chamber influences physical parameters. The properties influence crystallinity, crystalline structure, oxygen vacancies, the deposition rate, the thickness, and the final stoichiometric values with the stoichiometric sum of *Ba, Sr, Ti* and O in the solid solution that makes up $Ba_xSr_{1-x}TiO_3$ [8-13]. This research work establishes a simple way of understanding the RFMCS depositions by means of sigmoidal profile between *Ba* and *Sr*, and the arithmetic relationship of the perovskites (ABO_3: 1:1:3) that interact to establish mathematical models fitted in the relationships to experimental data of *Ba/Sr, (Ba+Sr)/Ti, Ba/Ti, Sr/Ti*. These mathematical expressions as a whole establish unpublished valid hypotheses in the interpretation and understanding of the deposition kinetics that include the deposition of *Ti* and O_2 in the RFMCS. The values of the experimental discrete points are obtained of [14] see Table II.

2. Materials, methods, and samples preparation

Every target was subjected during 15 minutes of a pre-sputtering process. When 120 W was applied to the STO target and simultaneously 0 W was applied to the BTO target then STO films (x=0) were obtained. The inverse procedure was used to obtain BTO thin films (x=1). To get values in the $0 \leq x \leq 1$ interval for the BST films 15 W of difference was applied on STO and BTO targets in steps in a complementary form, always keeping the total RF-magnetron applied power to both targets at 120W. See Table 2.

Table 1. Working parameters.

Concepts	Description and values
Targets	$BaTiO_3$ (BTO) and $SrTiO_3$ (STO); 2"x 0.125" with a purity of 99.95% (SCI Engineered Materials, Inc).
Deposition process	RF-Magnetron Co-Sputtering (RFMCS)
Substrate	Nichrome
Substrate temperature	In situ 495°C
Configuration	Off-axis 30°C
Distance substrate-magnetron	8 cm
Chamber evacuated pressure	$1.2X10^{-3}$ Pa
Flushing	3.9 Pa during 10 minutes
Rate gas mixture O_2/Ar	90/10
Pressure to ignite plasma	6.6 Pa
Pre-sputtering time (For cleaning targets)	15 minutes
Pressure working	3.9 Pa
Substrate rotation	100 rev/min
Stoichiometric content	EDS

Table 2. Configuration of applied power on both magnetron-targets.

Power Combination	RF-magnetron applied power (W)		Perovskite type
Name	BTO	STO	
APC1	0	120	STO
APC2	15	105	BST
APC3	30	90	BST
APC4	45	75	BST
APC5	60	60	BST
APC6	75	55	BST
APC7	90	30	BST
APC8	105	15	BST

APC9	120	0	BTO

3. Mathematical Model

Since the x values following the Boltzmann sigmoidal modified function, Equation (1) is proposed:

$$\mathrm{x}(P_i) = x_f - \frac{x_f - x_i}{1+e^{\frac{(\mathrm{P}-P_0)}{\alpha}}} \tag{1}$$

The first and second derivatives of Equation (1) is expressed by the following Equations (2 and 3).

$$\frac{\mathrm{d}}{\mathrm{d}P_i}x(P_i) = x'(P_i) = \frac{1}{\alpha}\left[\frac{(x_f - x_i)\, e^{\frac{(P_i-P_0)}{\alpha}})}{\left(1+e^{\frac{(P_i-P_0)}{\alpha}}\right)^2}\right] \tag{2}$$

$$\frac{\mathrm{d}^2}{\mathrm{d}{P_i}^2}x(P_i) = \mathrm{x}''(P_i) = -\frac{(x_f - x_i)\, e^{\frac{(P_i-P_0)}{\alpha}}}{\alpha^2\left(1+e^{\frac{(P_i-P_0)}{\alpha}}\right)^2}\tanh[\frac{P_i-P_0}{2\alpha}] \tag{3}$$

The first derivative has a maximum in the: $x(P_0) = \frac{(x_f+x_i)}{2}$; $x'(P_0) = \frac{(x_f-x_i)}{4\alpha}$. The second derivative can consider the minimum gradient value of the $x''(P_0) = 0$. [1,2,3].

4. Results and discussion

In Figure 1 for simple mathematical analysis and a broader understanding, it is convenient to establish the stoichiometric chemical relationship of a perovskite denoted by ABO_3, where *A* and *B* are the cations and oxygen is the anion. For our work, the cation *A* is formed by the *Ba+Sr* total atoms and cation *B* is the totality of *Ti* atoms, which is an ideal perovskite maintaining the following stoichiometric relationship with oxygen: ABO_3=1:1:3 or 20:20:60 expressed as a percentage. Then, from the mathematical point of view, this stoichiometric relationship is explained by two sigmoidal equations and the addition of two lines with slope equal to zero, to understand the experimental design.

Then it establishes that *Ba+Sr* = 20%, *Ti*=20%, and O_2=60%, therefore;

$$\mathrm{BST}(100\%) = 20(\%)\left[1 - \frac{1}{1+e^{\frac{(P_i-P_0)}{\alpha}}}\right] + \frac{20(\%)}{1+e^{\frac{(P_i-P_0)}{\alpha}}} + 20 * Ti(\%) + 60 * \mathrm{O}_2(\%) \tag{4}$$

where P_0= 45W and $\alpha = 18.05$ for calculating 20%*Ba* and P_0= 75W y $\alpha = 18.05$ for calculating 20%*Sr*, P_i=RF applied power on magnetron in every experimental discrete point. According to the experimental mathematical model, the straight dashes indicate the limits or lines with zero slope where the BST elements should converge for the sum of *Ba+Sr*, *Ti*, and oxygen, respectively, to obtain the BST_{100}. Note that in Figure 1, the increases and decreases of the relationships between the cations and anions of the experimental discrete points are indicated by asymmetric rectangles that indicate the variation between their deposition rates. These reasons are explained in relevant points and trends in detail, and which are explained in a general way from theory and what was found by other researchers, starting from the description of Figure 1 in combination with Figures 2, 3, and 4 of this manuscript. The Applied Power Combinations (APC) 0/120W (STO) and 120/0 (BTO) are analyzed below. It can be seen in Figure 1 that the applied power rates have a gap between the experimental values of the cations in relation to the anion, which is greater in the first applied power rate than in the second. In Figure 2b, the cations *Ba* and *Sr* for both applied powers remain below the expected percentage, but with very similar values in Figure 2c. *Sr* maintains in

better equilibrium with *Ti* than *Ba*; in fact, the imbalance between *Ba* and *Ti* is the most pronounced with a value of 3.13% lower than expected. In Figures 2(e) and 2(f) it is expected that APC1 and APC9 coincide with zero because only *Sr* and *Ba* are deposited respectively. However, as can be seen, *Sr* has a better control in the deposition for all APC than the *Ba*. In Figure 3, the *Sr/Ti* rate is very close to the ideal value, and the *Ba/Ti* rate is the furthest. Furthermore, the (*Ba*+*Ti*)/O rate is closer to the ideal value of the applied mathematical model.

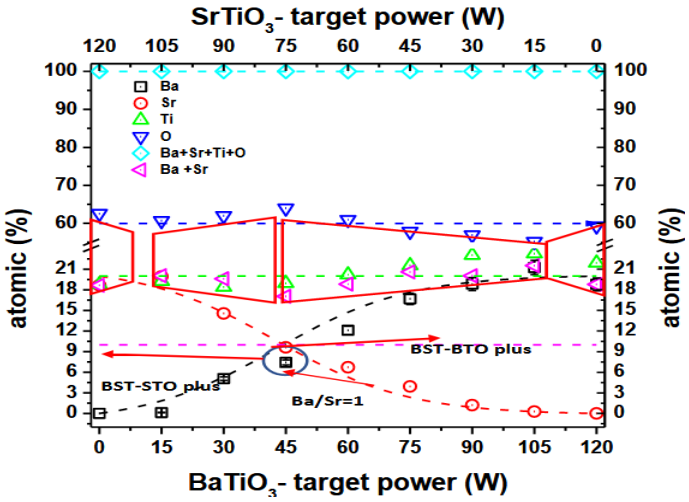

Fig. 1. Ba, Sr, Ti, and Oxygen percentage are plotted in BST with contents $0 \leq x \leq 1$ and that reflect the deviation with respect to a sigmoidal-linear mathematical model.

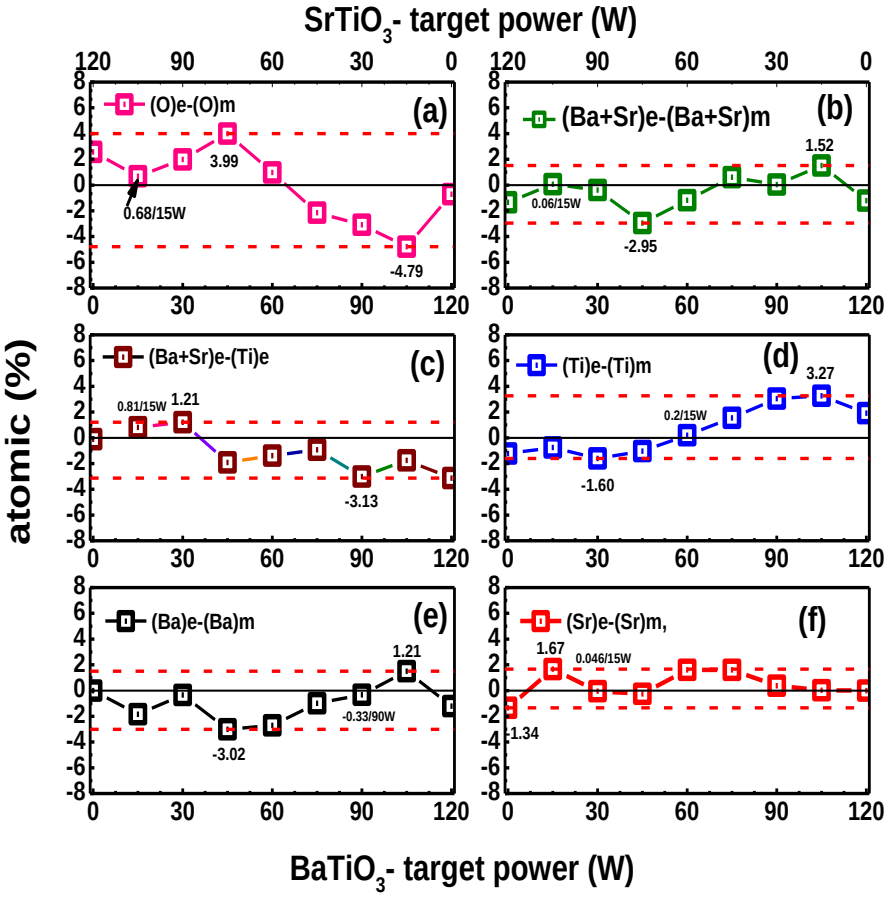

Fig. 2. Difference relationships between experimental and cations and anions model. The rate of difference between the experimental data and the proposed model for an ideal perovskite should be equal to zero in all cases.

In Figure 4, APC1 and APC9 are not shown for convenience of explanation of the BST. The cations and oxygen decrease and increase respectively from APC2 to APC4, which according to the experimental data and the S-profile of the BST deposition with a higher content of *Sr* reveal according to Figure 2a and 2d, to oxygen and cations above and below the expected percentage respectively. The (*A*+*B)*/O rate also remains below the ideal percentage expected according to Figure 3. The *Ba/Sr* rate in Figure 4 remains at very small values close to unity. APC 4, according to Figure 1 is the inflection point. The *Ba/Sr*=1 rate should take place and the value of *Sr* is the closest to 50% of the total percentage of cation *A* and where the gap between cations and anion is the largest. According to Figure 2a, oxygen has its maximum deviation value above the model and at the same time according to Figure 2b, the minimum value of *Ba*+*Sr* below the model. Furthermore, it is observed in Figure 2c that the difference ratio between the cations remains below the model from that point and is conserved in the other APC. According to Figure 2e the minimum value below the S-profile is the percentage of *Ba* and *Sr* very close to the expected value according to Figure 2f. According to Figure 3 the rate (*Ba*+*Sr*)/*Ti* obtains the minimum value below the mathematical model. From APC4 to APC8, the ratio between cations and oxygen tends to rise. This is the area where the substitution of *Ba* and *Ti* become predominant in the BST (see Figures 2d, 2e, and 3) while the *Sr* tends to stabilize with respect to the S-profile. In Figure 2a, the oxygen content begins to drop and reaches its lowest point, right at APC8, where the BST ends its deposition. In Figures 2c and 3, it is observed that the rate (*Ba*+*Sr*)/*Ti* remains below the expected value.

5. General explanation with the help of the mathematical model

This section explains in a technical way the whole trends previously described. The combination of the total working pressure, the applied power on two magnetrons, and the sputtering yield of the Ar^+ ions with the Ar/O_2=90/10 rate of our experiment is enough to achieve that the oxygen is integrated into the film as it happens in the APC where the applied power is greater in the STO target. This also obtains the closest values of the cations *A* and *B* of the ideal perovskite. Furthermore, it does not work where the APC are applied with the greatest applied power to the BTO target, where the values of cations *A* and *B* and oxygen are more dispersed than the ideal values. When the atomic mass of the target is greater, an Ar^+ ion hits the target with greater energy, so in the case of the STO and BTO targets the atomic masses are 183.490 g / mol and 233.192 g / mol, respectively. Therefore, as is expected Ar^+ ions impact the BTO target with greater kinetic energy. The differences found in the percentages of cations and oxygen in the change between APC, may be due to the fact, that there are greater dissociations of the covalent bonds between *Ti* and oxygen by means of the impact of more energetic ions where APC is greater on the applied power on BTO target following the principle, $XY + e \rightarrow (XY^-)$. Under low-pressure conditions, the above process is often followed by dissociation of the excited complex: $(XY^-) \rightarrow X + Y^-$. This dissociative attachment process is accepted as the major formation mechanism of negative ions in the low-pressure plasma, producing greater erosion and target surface oxidation [15]. Negative oxygen ions are generated when highly oxidative targets are bombarded. This intense sputtering yield of ions is considered the result of highly oxidative targets that are generated in the cathode sheath and plasma circumcising edges. [16,17]. Therefore, the formation of O^- ions that collide mostly with the Ar^+ ions, preventing their arrival to the substrate, is very likely. In addition, the O^- ions increase their kinetic energy when the applied power on target increases, thus allowing more collisions with ions Ar^+ [18]. In contrast, *Ti* ions and molecules with positive dipole moment travel without any restriction to the substrate for film deposition to take place. The collisions are between negative and positive O ions at the cathode sheath threshold and the plasma boundary. At the same time, inelastic collisions are likely in APC with higher applied power on BTO target, allowing the implantation of Ar ions and, on the contrary, inelastic

collisions are greater in APC when the applied power increases on the STO target, allowing physical momentum transmission.

The proposed mathematical model develops the following expressions:

$$Ba(\%) + Sr(\%) = Ti(\%) \tag{5}$$

$$\frac{Ba(\%)}{Sr(\%)} = \frac{Ti(\%) - Sr(\%)}{Sr(\%)} = e^{\frac{(P_i - P_0)}{\alpha}} \tag{6}$$

$$\mathrm{x}(P_i) = 1 - \frac{20}{1 + e^{\frac{(\mathrm{P}-45)}{18.05}}} \tag{7}$$

$$[x(P_i)]' = \frac{1}{18.05}\left[\frac{20\, e^{\frac{(P_i-45)}{18.05}}}{\left(1 + e^{\frac{(P_i-45)}{18.05}}\right)^2}\right] \tag{8}$$

$$[x(P_i)]'' = -\frac{20\, e^{\frac{(P_i-45)}{18.05}}}{(18.05)^2\left(1 + e^{\frac{(P_i-75)}{18.05}}\right)^2}\tanh\left[\frac{P_i - 45}{36.10}\right] \tag{9}$$

$$1 - \mathrm{x}(P_i) = \frac{20}{1 + e^{\frac{(\mathrm{P}-75)}{18.05}}} \tag{10}$$

$$[1 - x(P_i)]' = \frac{1}{18.05}\left[\frac{20\, e^{\frac{(P_i-75)}{18.05}}}{\left(1 + e^{\frac{(P_i-75)}{18.05}}\right)^2}\right] \tag{11}$$

$$[1 - x(P_i)]'' = -\frac{20\, e^{\frac{(P_i-45)}{18.05}}}{(18.05)^2\left(1 + e^{\frac{(P_i-75)}{18.05}}\right)^2}\tanh\left[\frac{P_i - 75}{36.10}\right] \tag{12}$$

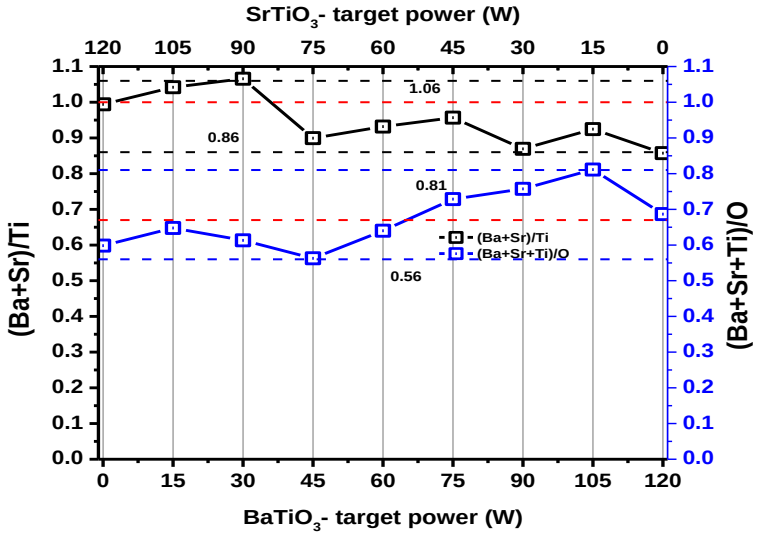

Fig. 3. The A/O and (A+B)/O rates are graphed. The dashed red lines indicate the value that the rates should be according to the model and the dashed black lines indicate the limit values of the rates below and above the model value.

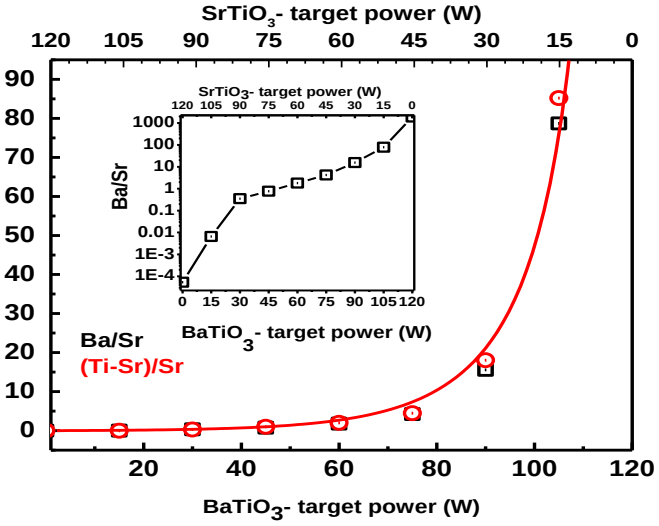

Fig. 4. The Ba/Sr rate is plotted as an applied power function and its fit to an exponential function. The red figures show the rate expected value according to the proposed model. The inset is plotted with experimental values on a logarithmic scale.

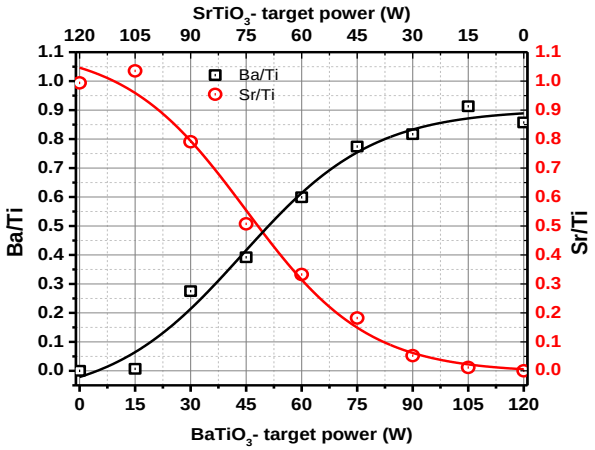

Fig. 5. The Ba/Ti and Sr/Ti rates maintain a S-profile with extremes that not achieve the 100%.

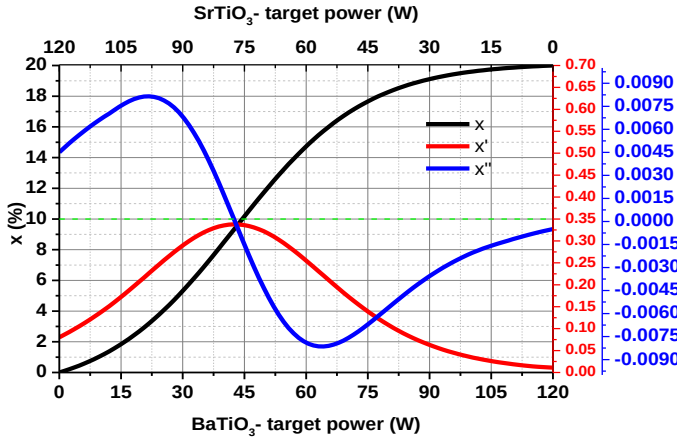

Fig. 6. x, x' and x'' are plotted as a function of the content of Ba (x), and as a function of the applied power.

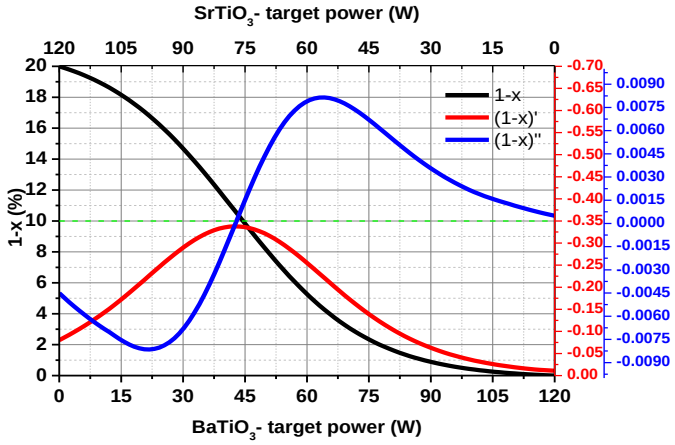

Fig. 7. (1-x)' and (1-x)'' are plotted as a function of the Sr (1-x), and also as a function of the applied power.

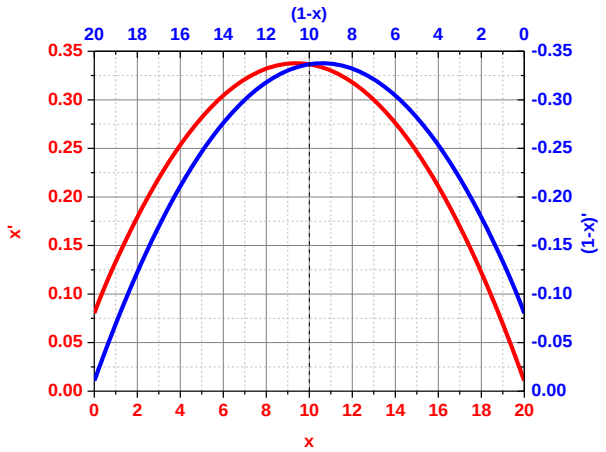

Fig. 8. x' vs x and (1-x)' vs (1-x).

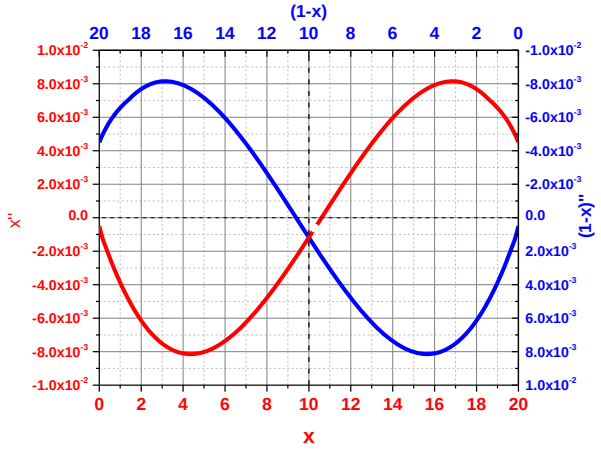

Fig. 9. x'' vs x and (1-x)'' vs (1-x)

Figure 4 plots the *Ba/Ti* and *Sr/Ti* rates with experimental values (black squares) and with model values (red circles). These rates are only presented up to APC8 (so that it is not undetermined) and it verifies that the rates between the cations *A* are of the exponential type as verified in Equation 6. It is well known that when the applied power increases on the target of BTO, and decreases on the STO target, after an inflection point in the APC, the sputtering yield of *Ba* increases due to the difference in atomic masses in the system (*Ba* =137.33u, *Sr* = 87.62 u, *Ti* = 47.867 u, O_2 = 15.999 u). Hence it follows that the *Ba/Sr* rate has this trend.

Figure 5. The mathematical model proposed develops the following expressions:

$$\frac{Ba(\%)}{Ti(\%)} = \frac{e^{\frac{(P_i - P_0)}{\alpha}}}{1+e^{\frac{(P_i - P_0)}{\alpha}}} \text{ and } \frac{Sr(\%)}{Ti(\%)} = \frac{1}{1+e^{\frac{(P_i - P_0)}{\alpha}}}$$

These uses are the same tan S-profile fit of the Boltzmann equation to *Ba/Ti* and *Sr/Ti* rates.

Figures 6 and 7 plot the x, 1-x, first derivative x', (1-x)', second derivative x'', (1-x)'' as a function of applied power in RFMCS that are represented by means of Equation 1, Equation 2 and Equation 3 respectively. These results are very consistent between the proposed model, and the stoichiometric measurements method were performed with XRD reported in [2].

Figure 8, it can be noted that the profile that is drawn for x' vs x, that is, the rate of change in the content of x in the BST, is parabolic, and its minimum value coincides with the deposition of STO and BTO, where the sputtering yield is maximum. In Figure 9, an asymmetric sinusoidal profile is drawn if one starts from the point where the ratio *Ba/Sr*=1 and that reflects the asymmetry of the APC proposed for the experiment and which can show the speed-up rate of ions and molecules towards the substrate.

6. Conclusions

The mathematical model proposed to describe the kinetics of the BST/nichrome deposition of the interval $0 \leq x \leq 1$ in *Ba* and *Sr*, establishes that there is a direct relationship between the content of cations and oxygen as a function of the RFMCS applied power. The knowledge of the exponential profiles of the *Ba/Sr* and sigmoid rate of *Ba/Ti* and *Sr/Ti*, and the described relationship of the kinetics of ions and molecules can contribute to establishing the setup of working conditions in a complementary way to other mathematical models that start from what happens in the RFMCS. This does not take into account what happens in the data obtained from the content of the cations and anions of the perovskite in the substrate. Among these conditions, the Ar/O_2 rate plays an important role to control, in a simple but effective way, the content of cations *A* and *B*, and of the oxygen anion in perovskite and perhaps in general in quaternary materials where the target is highly oxidative.

References

[1] J. Reséndiz-Muñoz, M. A. Corona-Rivera, J. L. Fernández-Muñoz, M. Zapata-Torres, A. Márquez-Herrera, V. M. Ovando-Medina, Bulletin of Materials Science 40(5), 1043 (2017); https://doi.org/10.1007/s12034-017-1441-x

[2] J. Reséndiz-Muñoz, J. Estrada-Martínez, M. A. Meléndez-Lira, O. Zelaya-Ángel, J. D. J. Medel-Juárez, F. Caballero-Briones, J. L. Fernández-Muñoz, Coatings, 8(10), 362 (2018); https://doi.org/10.3390/coatings8100362

[3] K. A. Cruz, J. M. Juárez, M. Z. Álvarez, R. P. Orozco, F. Caballero-Briones, J. L. Fernández-Muñoz, Digest Journal of Nanomaterials and Biostructures, 15(1), 33 (2020).

[4] J. Resendiz-Munoz, J.L. Fernandez-Munoz, M.A. Corona-Rivera, M. Zapata-Torres, A. Marquez-Herrera, M. Melendez-Lira, Journal of Nanomaterials, Article ID 4308294, 8 pages

(2017); https://doi.org/10.1155/2017/4308294

[5] J. Reséndiz-Muñoz, J.L. Fernandez-Munoz, J. R. Farias-Mancilla, M. Meléndez-Lira, J. J. Medel-Juárez, O. Zelaya-Angel, Digest Journal of Nanomaterials and Biostructures, 3(3) 751 (2018).

[6] O. Zelaya-Angel, M. Melendez-Lira, J. Reséndiz-Muñoz, J. L. Fernández-Muñoz, F. Caballero-Briones Mater. Res. Express 7(4),046402 (2020); https://doi.org/10.1088/2053-1591/ab81bd

[7] J. L. Estrada-Martínez, J. A. Melo-Banda, U. Páramo-García, J. Reséndiz-Muñoz, J. L. Fernández-Muñoz, M. Meléndez-Lira, O. Zelaya-Ángel, Preprints, 2017100043 (2017); https://doi.org/10.20944/preprints201710.0043.v1

[8] Y. Wang, B. Liu, F. Wei, Z. Yang, J. Du, Journal of alloys and compounds 475(1-2), 827 (2009); https://doi.org/10.1016/j.jallcom.2008.08.012

[9] T. Bayrak, C. Ozgit-Akgun, E. Goldenberg, Journal of Non-Crystalline Solids, 475, 76 (2017); https://doi.org/10.1016/j.jnoncrysol.2017.08.036

[10] M. Tarutani, M. Yamamuka, T. Takenaga, T. Kuroiwa, T. Horikawa, Thin Solid Films 409(1), 8 (2002); https://doi.org/10.1016/S0040-6090(02)00095-0

[11] A. A. Camacho-Berríos, V. M. Pantojas, W. Otaño, Thin Solid Films 692, 137641 (2019); https://doi.org/10.1016/j.tsf.2019.137641

[12] M. S. Tsai, S. C. Sun, T. Y. Tseng, Journal of Applied Physics 82(7), 3482 (1997); https://doi.org/10.1063/1.365665

[13] F. Alema, A. Reinholz, K. Pokhodnya, Journal of Applied Physics, 114(17), 174104 (2013); https://doi.org/10.1063/1.4829000

[14] A. Márquez-Herrera, E. Hernández-Rodríguez, M. P. Cruz, O. Calzadilla-Amaya, M. Meléndez-Lira, J. Guillén-Rodríguez, M. Zapata-Torres, Revista mexicana de física 56(5), 401 (2010).

[15] E. Stoffels, W. W. Stoffels, V. M. Kroutilina, H. E. Wagner, J. Meichsner, Journal of Vacuum Science & Technology A: Vacuum, Surfaces, and Films 19(5), 2109 (2001); https://doi.org/10.1116/1.1374617

[16] K. Tominaga, T. Kikuma, K. Kusaka, T. Hanabusa, Vacuum 66(3-4), 279 (2002); https://doi.org/10.1016/S0042-207X(02)00155-0

[17] M. Zeuner, H. Neumann, J. Zalman, H. Biederman, Journal of applied physics 83(10), 5083 (1998); https://doi.org/10.1063/1.367325

[18] T. Ishijima, K. Goto, N. Ohshima, K. Kinoshita, H. Toyoda, Japanese Journal of Applied Physics 48(11R), 116004 (2009); https://doi.org/10.1143/JJAP.48.116004